Gate tunable photovoltaic effect in MoS_2 vertical p–n homostructures†

Simon A. Svatek, Elisa Antolin, Der-Yuh Lin, Riccardo Frisenda, Christoph Reuter, Aday J. Molina-Mendoza, Manuel Muñoz, Nicolás Agraït, Tsung-Shine Ko, David Perez de Lara and Andres Castellanos-Gomez

p–n junctions based on vertically stacked single or few-layer transition metal dichalcogenides (TMDCs) have attracted substantial scientific interest. Due to the propensity of TMDCs to show exclusively one type of conductivity, n- or p-type, heterojunctions of different materials are typically fabricated to produce diode-like current rectification and photovoltaic response. Recently, artificial, stable and substitutional doping of MoS_2 into n- and p-type materials has been demonstrated. MoS_2 is an interesting material for use in optoelectronic applications due to its potential of low-cost production in large quantities, strong light–matter interactions and chemical stability. Here we report the characterization of the optoelectronic properties of vertical homojunctions made by stacking few-layer flakes of MoS_2:Fe (n-type) and MoS_2:Nb (p-type). The junctions exhibit a peak external quantum efficiency of 4.7% and a maximum open circuit voltage of 0.51 V; they are stable in air; and their rectification characteristics and photovoltaic response are in excellent agreement with the Shockley diode model. The gate-tunability of the maximum output power, the ideality factor and the shunt resistance indicate that the dark current is dominated by trap-assisted recombination and that the photocurrent collection depends strongly on the spatial extent of the space charge region. We demonstrate a response time faster than 80 ms and highlight the potential to integrate such devices into quasi-transparent and flexible optoelectronics.

Introduction

Two-dimensional layered materials offer a broad variety of building blocks with remarkable electronic, photonic and mechanical properties.[1] In particular, TMDCs, such as WSe_2 and MoS_2, are considered as promising candidates for photovoltaic devices due to their strong light–matter interactions[2–4] and tunable (thickness-dependent) band gaps.[5,6] There is a growing number of fundamental[7–10] and applied[11–13] studies on thin layers of MoS_2. However, the formation of photovoltaic devices exclusively made of MoS_2 is hampered by the lack of samples with both transport characteristics, n-type and p-type, since MoS_2 typically exhibits only n-type doping. Previous experimental efforts to form junctions have therefore focused on layered heterojunctions formed by vertical van der Waals stacking of dissimilar materials, mostly in combination with WSe_2,[14–17] and less frequently with other compounds such as GaTe,[18] black phosphorus,[19] and graphene.[20,21] Besides, the possibility of forming homojunctions from MoS_2 has been explored with promising results, but this could only be realised through superficial doping by exposing devices after processing to $AuCl_3$,[22,23] through Schottky junctions,[24] or through local electrostatic gating.[25–28] Recently, stable p-type conduction by substitutional niobium doping has been demonstrated in MoS_2,[29] which enables the formation of all-MoS_2 p–n junctions. Here we demonstrate that, by fabricating MoS_2 homostructures from the vertical van der Waals assembly of p-type MoS_2 (0.5% Nb doping, $\sim 3 \times 10^{19}$ cm^{-3}) and n-type MoS_2 (either 0.5% Fe doping, or native n-type material), we can create solar harvesting p–n junctions. By fitting the current–voltage characteristics of these junctions with the Shockley diode model

at various gate voltages, we extract all diode parameters and analyse in detail their gate dependence.

The underlying physical mechanisms of rectification and photovoltaic response in vertical TMDC heterojunctions are fundamentally different from the mechanisms governing conventional p–n junctions based on the concept of selective contacts. It has been proposed[30] and experimentally shown[17,31] that in monolayer MoS_2/WS_2 heterojunctions, the photovoltaic response and current–voltage characteristics are governed by the interlayer tunnelling recombination of majority carriers and do not follow an exponential law.[17] The rectification is a result of the type-II band alignment with given band offsets for electrons and for holes. The maximum achievable photovoltage is limited by the smallest of these offsets, which in the case of MoS_2/WSe_2 is the band offset for electrons, approximately 0.7 eV.[30] In contrast, in conventional p–n junctions, selective contacts for electrons and holes are produced through p- and n-doping and the electrical characteristics are determined by drift and diffusion processes of minority carriers. The photovoltage is limited by the built-in field which in turn is limited by the material bandgap, which typically exceeds the band offsets in heterojunctions. In the case of bulk MoS_2, the direct band-gap is 1.8 eV and the indirect band-gap is 1.3 eV.[6] This consideration is crucial when assessing the potential of TMDC-based devices for solar applications, and it emphasizes the need to explore vertical devices comprising selective contacts produced by stable atomic doping of TMDCs. In this work, we present the characterization of vertical MoS_2 p–n homojunctions in the intermediate thickness regime (15–19 nm) between the monolayer and the bulk. We demonstrate that the current–voltage characteristics are in excellent agreement with the Shockley diode model, implying that the carrier dynamics in our MoS_2 homojunctions is predominantly governed by drift and diffusion processes. Ideality factors around 2.5 indicate trap-assisted recombination in the depleted regions. The performance of the devices is substantially affected by the gate voltage (V_G) through the modulation of the carrier densities and the electric field at the junction. In particular, a positive effect of V_G on the open-circuit voltage (V_{OC}) is always accompanied by a negative effect on the short-circuit current (I_{SC}) which points to a carrier collection influenced by the spatial extent of the space charge region. Interestingly, not only the ideality factor and the reverse saturation current but also the parasitic shunt resistance are modulated by the gate, suggesting that tunnel-assisted recombination is still relevant in devices of moderate thickness ($\sim$15 nm).

Results and discussion

MoS_2:Nb and MoS_2:Fe single crystals were grown by the chemical vapour transport method described by Wang *et al.*[32] and Suh *et al.*[29] (for an exhaustive study of the material composition, see ref. 29). Thin flakes of about 10 to 10^3 μm^2 in size were prepared by micromechanical exfoliation of bulk crystals and deposited onto a viscoelastic stamp (GelFilm by GelPak).[33] Upon optical inspection a flake was transferred onto an Au/Ti (40 nm/10 nm) metal lead on a 295 nm SiO_2/Si substrate by pressing the viscoelastic stamp onto the substrate and releasing it slowly. Fig. 1a and b show schematically the fabrication steps along with the optical images of the device. First, the n-type flake was deposited onto the substrate, partially overlapping with an Au/Ti (40 nm/10 nm) metal contact. Subsequently a p-type flake was transferred using the same method, overlapping with the first flake to form a vertical junction. The thicknesses of the flakes were determined to be 9 nm (MoS_2:Nb) and 6 nm (MoS_2:Fe) by atomic force microscopy.

We recorded the current density (J) as a function of the source–drain voltage (V_{SD}) and the V_G. All measurements have been performed under ambient conditions. Fig. 1c shows the J–V_{SD} characteristics of the p–n (MoS_2:Nb–MoS_2:Fe) homojunction in the dark and under illumination with monochromatic light (λ = 660 nm, intensity 80 mW cm^{-2}) at various V_G values. We observe rectifying J–V_{SD} characteristics in the dark and photovoltaic behaviour under illumination. The photoresponse characteristics are modulated by the Si-gate electrode by changing the charge carrier density. The generated electrical power density $P_{el} = J\ V_{SD}$ for various V_G values is shown in Fig. 1d. A maximum of P_{el} = 0.42 mW cm^{-2} and V_{OC} = 0.51 V is generated at $V_G = -30$ V. This exceeds the reported V_{OC} values at similar intensities of van der Waals heterojunctions made of MoS_2/WSe_2,[9,17] MoS_2/GaTe,[18] and MoS_2/black phosphorous,[19] although it exceeds that of the graphene/MoS_2/WSe_2/graphene junction[17] due to enhanced extraction. Each J–V_{SD} trace in Fig. 1c has been fitted independently using a circuital model. It comprises a Shockley-diode and parasitic resistances in series (R_S) and in parallel (R_P), and it is described using the equation: $J = J_0\left(\exp\left(\frac{e(V_{SD} - JR_S)}{nkT}\right) - 1\right) + \frac{V_{SD} - JR_S}{R_P} - J_L$, where k is the Boltzmann constant, e is the electron charge, T is the temperature, n is the ideality factor, J_0 is the reverse saturation current density of the diode and J_L is the photogenerated current density. The fits are overlaid in Fig. 1c as solid lines, showing a strong agreement between the experimental data and the Shockley model. The parameters n, J_0, J_L, R_S, and R_P that optimize each fitting are collectively plotted in Fig. 2, and behave as continuous functions of V_G.

The agreement between the data and the Shockley-diode model implies that carrier dynamics can be explained by the presence of a built-in field $E_{built\text{-}in}$ and the associated space charge region and neutral regions. This is illustrated in an ideal band diagram, see Fig. 1e, in which the space charge region is represented as the grey area. Note that only the junction area, highlighted with dotted lines in Fig. 1b, is considered in the band diagram. In our devices, drift and diffusion of minority carriers exclusively take place in the junction area, and the space charge region does not spread horizontally beyond. This implies that none of the observed effects originates from parasitic Schottky junctions at the contacts (further discussion is provided below regarding Fig. 6).

The presence of a gate voltage ($V_G \neq 0$ V) produces either depletion or accumulation in the carrier population of the flakes and causes an additional field E_{Gate} parallel to the built-in field

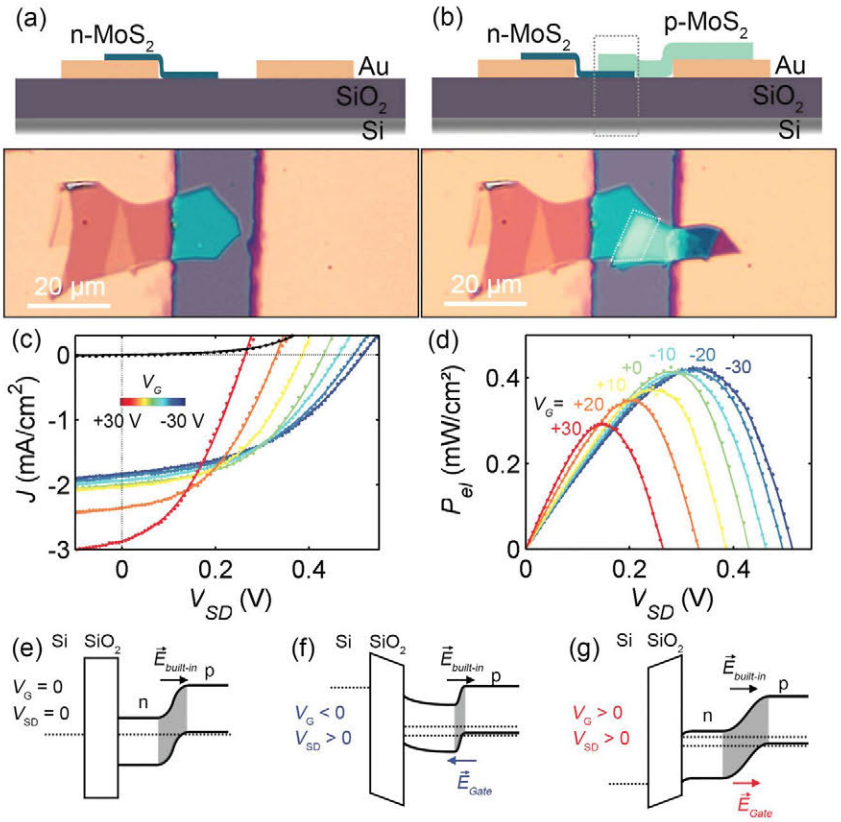

Fig. 1 Device schematic and optical images of the n-type MoS_2 flake on top of Au/Ti lead before (a) and after (b) the transfer of the p-type MoS_2. The dotted lines indicate the junction area. (c) J–V_{SD} curves taken under illumination with λ = 660 nm at 80 mW cm^{-2} at gate voltages from +30 V to −30 V in 10 V steps (black: J–V_{SD} curve in the dark at V_G = 0 V). Experimental data are depicted as points, and fits assuming the Shockley diode model are overlaid. (d) The generated electrical power density P_{el} against V_{SD} at various V_G values. (e–g) Band diagrams of the junction area at various V_G values. The dotted lines represent the quasi Fermi levels for electrons and holes. The space charge region is highlighted in grey. V_G introduces an electric field E_{Gate} which enhances or reduces the total field and therefore contributes to band bending.

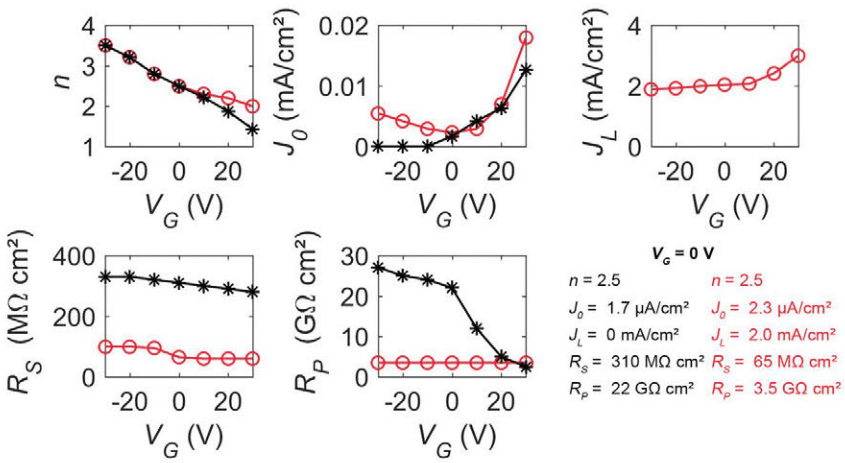

Fig. 2 Fitting parameters extracted from Shockley-model fits, see Fig. 1 and Fig. S1 (ESI†). Red circles correspond to parameters under illumination (λ = 660 nm at 80 mW cm^{-2}), and black stars correspond to parameters in the dark.

$E_{built\text{-}in}$ at the junction (Fig. 1f and g), which alters the band bending and the relative position of the bands with respect to the Fermi level. For negative V_G, the n-MoS_2 tends to be depleted, the p-MoS_2 accumulates carriers, and $E_{built\text{-}in}$ is reduced by E_{Gate}. This is accompanied by a reduction of the thickness of the space charge region since the density of ionized dopant atoms which provide the field is predetermined by doping. A positive V_G has the opposite effects. Thus, the thickness of the space charge region grows with V_G. The band bending introduced by E_{Gate} resembles a forward source–drain bias for negative V_G and *vice versa*.

In our device the p-MoS_2 is expected to be degenerate,[29] which implies that the carrier accumulation or depletion takes place mostly in the n-MoS_2. This has been taken into account in Fig. 1f and g, where the Fermi level appears pinned to the valence band in the p-type region.

The modulation of the thickness of the space charge region by V_G affects the J–V_{SD} characteristics plotted in Fig. 1c and thereby the fitting parameters from the Shockley-diode model, which are presented in Fig. 2. The ESI† contains gate-dependent J–V_{SD} characteristics in the dark (Fig. S1, ESI†). Ideality factor values in the range n = [2–3.5] are indicative of recombination mechanisms that become less efficient as V_{SD} increases. Such recombination is associated with coupled defects and possible tunnelling mechanisms,[34,35] which most likely occur in the space charge region where defects are not saturated and where the electric field can enhance the tunnelling processes. The dramatic increase of n with decreasing V_G in our devices is consistent with tunnelling-assisted recombination at traps in the space charge region since tunnelling becomes less effective as the total field in the junction is reduced. It has to be noted that the depleted regions generated by V_G at the MoS_2/SiO_2 interface do not necessarily contribute to this recombination because carriers are prevented to approach the MoS_2/SiO_2 interface by the presence of depleting fields. The amount of recombination, characterized by J_0, increases with V_G and thus with the thickness of the space charge region. The dark current, open-circuit voltage and power densities improve with decreasing V_G, mostly due to the increase of n and the decrease of J_0.

The parameter J_L is the photogenerated current when no voltage is applied across the junction. Under those circumstances, there can be no quasi-Fermi level split in the space charge region and therefore recombination can only take place in the rest of the device. Hence, J_L accounts for the total photogenerated electron–hole pairs reduced by the recombination that takes place in the volume which is not occupied by the space charge region under short-circuit conditions.[36] Consequently, J_L increases with V_G. The absolute value of J_L in our devices is in the range [1.9–3.0 mA cm^{-2}].

Interestingly, the fittings yield different R_P values in the dark and under illumination. In the dark, R_P shows a strong dependence on V_G. R_P quantifies local shuntings in the space charge region caused by tunnelling processes at coupled defects which is a known mechanism in conventional solar cells with high trap densities and $n > 2$.[35] As above, the tunnelling is enhanced when the total field is increased by V_G, which leads to a decrease in R_P. Under illumination, we find a constant R_P independent of the gate. This is an apparent R_P related to a modulation of the photogenerated current and not to shunting. It reflects an increase of the photogenerated current with a decrease in V_{SD}, which occurs due to the enlargement of the space charge region (similar to the case of the positive V_G discussed above). This is known from other technologies of very thin solar cells, such as CdTe and chalcopyrite-based devices, in which the space charge region occupies a significant part of the total volume, and it is known as voltage-dependent collection.[37]

The series resistance R_S of the flakes depends on the occupation levels. As V_G increases, the Fermi level is shifted towards the conduction band causing the resistance of the n-type (or p-type) flake to decrease (or increase). In the p–n junction, we observe a decrease of the resistance with an increasing V_G which implies that the gate-dependence of the n-type flake is predominant. This can be attributed to the degenerate doping of the p-flake, the lower thickness of the n-type flake and a gate-screening effect, due to which the p-type flake is not effectively controlled by V_G since the n-type flake is screening the electric field. R_S shows the same gate-dependence in the dark and under illumination. When illuminated, R_S is smaller than in the dark because of a higher overall population. The values are in the range [60–100 MΩ] under illumination and [280–330 MΩ] in the dark.

Fig. 1d shows that the positive effect of V_G on the photogenerated current is counteracted by the opposite effect on photovoltage, causing P_{el} to increase as V_G decreases. The previous

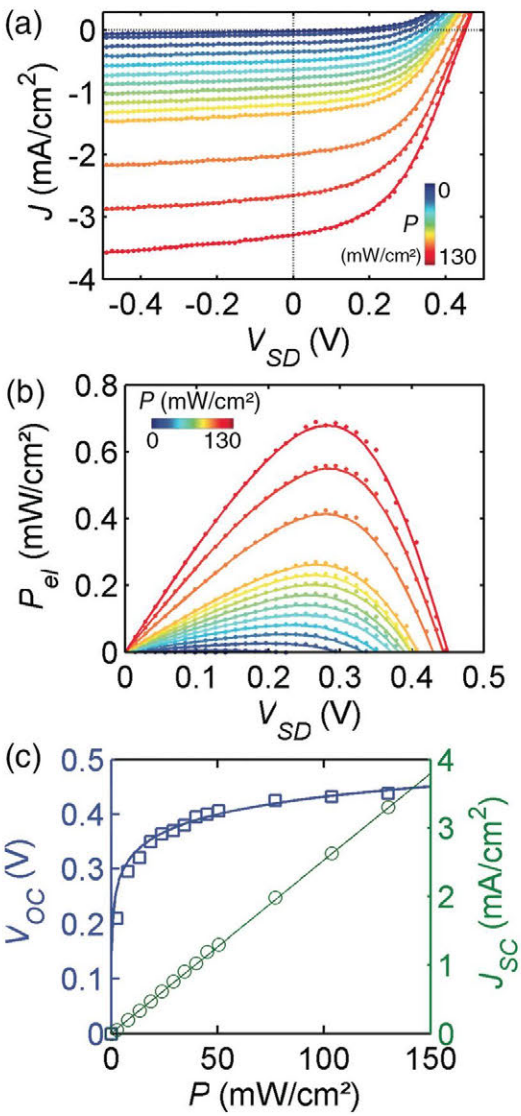

Fig. 3 Device characteristics under illumination with λ = 660 nm at V_G = 0 V. The incident power ranges from 0 to 130 mW cm^{-2}. (a) Power dependence of J–V_{SD} characteristics. (b) Incident power dependence of the electrical power density P_{el} *vs.* V_{SD}. (c) Logarithmic (linear) power dependence of V_{OC} (J_{SC}) extracted from (a).

analysis allows us to attribute both effects to the modulation of the space charge region. This result differs fundamentally from the behaviour of heterojunction-based WSe_2/MoS_2 devices, where a variation in V_G affects directly the amount of interlayer recombination and leads to either an increase of photovoltage and photocurrent, or the reduction of both.[17] Note that the device performance does not improve indefinitely since V_G introduces non-linear effects in the series resistance of the flakes leading to the junction. Such behaviour is more pronounced in a MoS_2:Nb–native MoS_2 junction, see the ESI,† Fig. S3.

Fig. 3a and b show the dependence of the J–V_{SD} characteristics and P_{el} on the incident power with above-bandgap illumination (λ = 660 nm). The electrical power density reaches a maximum of 0.68 mW cm^{-2}. The maximum in short-circuit current is J_{SC} = 3.3 mA cm^{-2} which corresponds to an external quantum efficiency of EQE = 4.7% and a responsivity of 25 mA W^{-1}, which is similar to what has been achieved in a vacuum in MoS_2 homojunctions made by surface doping (30 mA W^{-1}).[22] A fill factor (FF) of 0.46 has been determined from max(P_{el}) = $V_{OC}J_{SC}$ FF. The dependences of V_{OC} (Fig. 3c, left axis, blue squares) and J_{SC} (right axis, green circles) are, respectively, logarithmic and linear on the incident power, which demonstrates that the J–V_{SD} characteristics are dominated by the Shockley-diode despite the presence of parasitic resistances. Besides, this confirms that the photocurrent is predominantly caused by the photovoltaic effect as opposed to thermoelectric effects.[28]

By recording the photoresponse for various illumination wavelengths, we characterize the junction further. Fig. 4a shows J–V_{SD} characteristics for wavelengths between 405 nm and 1050 nm. The response has a peak in the vicinity of the exciton energies 659 nm and 611 nm (in monolayer materials),[38] where the optical absorption is enhanced. For photons with higher wavelengths, $\lambda \geq 850$ nm, the device shows a negligible response, which is due to the reduced absorption of the indirect bandgap transitions. The response for wavelengths between 455 nm and 660 nm corresponds to EQEs which range from 1.6% to 4.5%.

To determine the switching speed, we recorded the J against the time while the illumination (λ = 660 nm, intensity 80 mW cm^{-2})

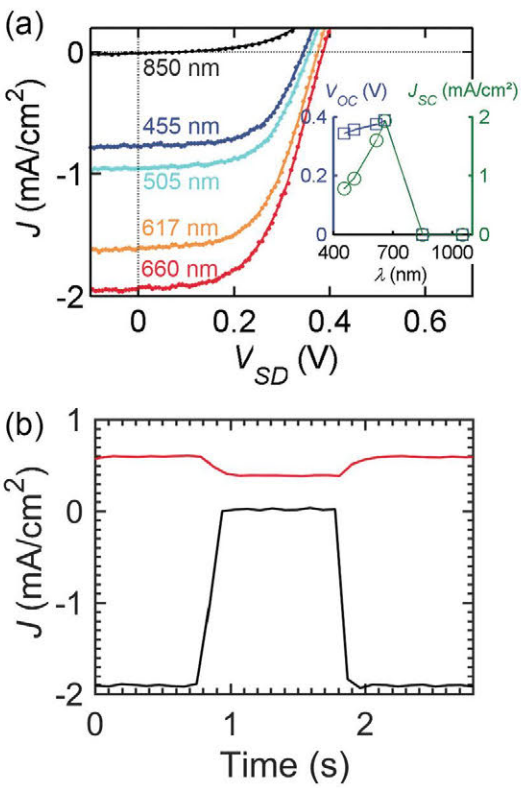

Fig. 4 (a) J–V_{SD} curves at different illumination wavelengths at 80 mW cm^{-2}. The device shows no photoresponse at wavelengths $\lambda \geq 850$ nm. The inset shows the dependence of V_{OC} and J_{SC} on the wavelength. (b) Current density across the device against time at V_G = 0 V. The illumination (80 mW cm^{-1} at λ = 660 nm) was alternatingly turned on and off. Under short-circuit conditions (black), we extract 80 ms as an upper limit for the response time. The response time at V_{SD} = 0.5 V (red) is determined as 180 ms.

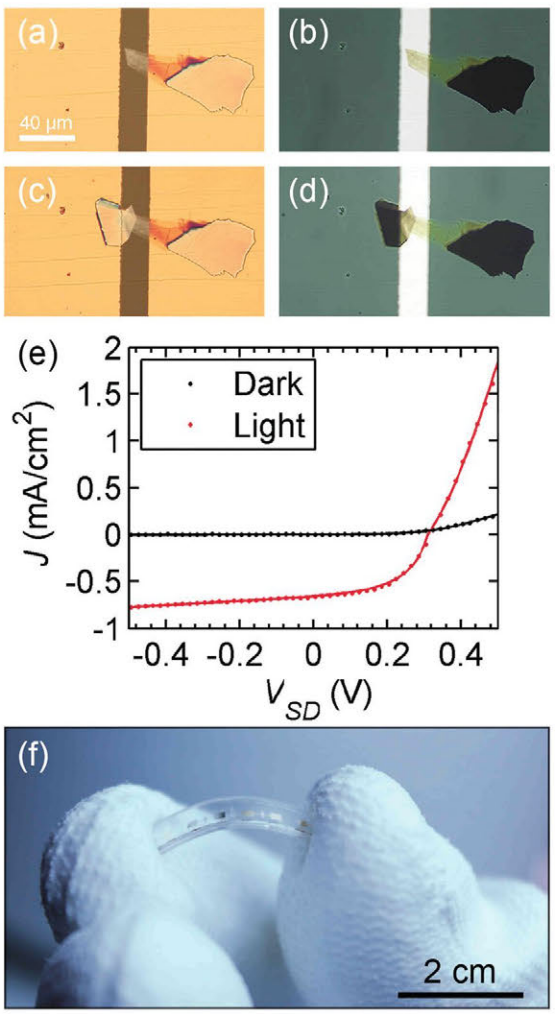

Fig. 5 (a)–(d) Optical images of a quasi-transparent device with MoS_2:Nb (a and b) and the MoS_2:Nb–MoS_2:Fe junction (c and d) in the bright field mode (a and c) and in the transmission mode (b and d) on a polycarbonate substrate with Au/Ti (70 nm/15 nm) leads. (e) J–V_{SD} curves in the dark and under illumination with λ = 660 nm and 80 mW cm^{-2}. Fits assuming the Shockley diode model are overlaid as solid lines. (f) A photograph of the device. The scale bar refers to the focal plane of the camera.

was alternatingly turned on and off (Fig. 4b). When the device is unbiased (black curve) we extract an upper limit of 80 ms for both the rise and decay times, which are defined as the time required for I to rise (fall) to 90% (10%) of the difference between the initial and final values. Note that this value is limited by our experimental setup. This temporal response is one order of magnitude faster than previously reported MoS_2 photodetectors with planar geometries,[39] however, 9 orders of magnitude slower than the values reported for graphene/TMDC/graphene devices.[40] The strong differences in response times can be attributed to the differences in the device geometries, carrier mobilities, flake thicknesses and extraction efficiencies. Response times in planar MoS_2 photodetectors are limited by the capacitance that is induced by trapped charge carriers. Faster response times in few-layer MoS_2 under ambient conditions ($\sim$10 ms) could, to our knowledge, only be realised by surface treatments, such as encapsulation with HfO_2.[41] Under forward bias conditions, V_{SD} = 0.5 V (red curve), the photoresponse comprises also a photoconductance mechanism and the response time has been determined as 180 ms. We conclude that the photovoltaic effect in this geometry is at least 100 ms faster than other reported values. In line with the results discussed earlier, our devices show a similar behaviour as conventional, selectively doped p–n junctions, in which the response time is dominated by diffusion mechanisms if operated in the photovoltaic mode and a forward bias introduces a drift current which increases the response time.[42]

We have also prepared a p–n (MoS_2:Nb–native MoS_2, 13 nm–6 nm) homojunction and compared it to the p–n (MoS_2:Nb–MoS_2:Fe) above. We find the same qualitative dependences of n, I_0, R_P, and R_S on the gate voltage. Under illumination with λ = 660 nm and an intensity of 80 mW cm^{-1}, the maximum power P_{el} = 0.04 mW cm^{-2} is generated at V_G = −10 V and at V_{SD} = 0.09 V. We extract V_{OC} = 0.14 V and FF = 0.4. J_{SC} = 0.64 mA cm^{-2} corresponds to EQE = 2.6% and a responsivity of 14 mA W^{-1}. We attribute the lower device performance to the lower doping level of the native MoS_2 in comparison to the intentionally doped MoS_2 (for additional data and a discussion of the doping levels, see the ESI†).

The van der Waals assembly technique allows us to easily form p–n junctions on virtually any substrate. Here, we explore the potential for transparent and flexible substrates. Fig. 5a–d show optical micrographs of a p–n (MoS_2:Nb–MoS_2:Fe, 10 nm–9 nm) homojunction on a polycarbonate substrate in reflection and transmission modes. We find that ~50% of the incident white light is transmitted through the electrodes. The transmittance of the device area varies in the range of 70 ± 15%, suggesting that our materials may be used in quasi-transparent applications. Fig. 5e shows the J–V_{SD} characteristics in the dark and under illumination of this flexible device. From circuit modelling we find n = 2.46, I_0 = 0.3 pA, R_S = 0.7 GΩ, and negligible R_P in the dark and n = 2.84, I_0 = 5.8 pA, R_S = 70 MΩ and R_P = 7 GΩ under illumination with λ = 660 nm at a power of 80 mW cm^{-2}. We extract the maximum power density P_{el} = 0.11 mW cm^{-2} at V_{SD} = 0.21 V. The other figures of merit are EQE = 1.5% and a responsivity of 8 mA W^{-1} for J_{SC} = 0.66 mA cm^{-2}, V_{OC} = 0.32 V, and FF = 0.51. After bending the substrate 50 times to a local radius of curvature of 2.5 cm (see Fig. 5f), the J–V_{SD} characteristics remain unaltered. The lower device performance as compared to devices on SiO_2/Si substrates may be attributed to the absence of a reflective background.

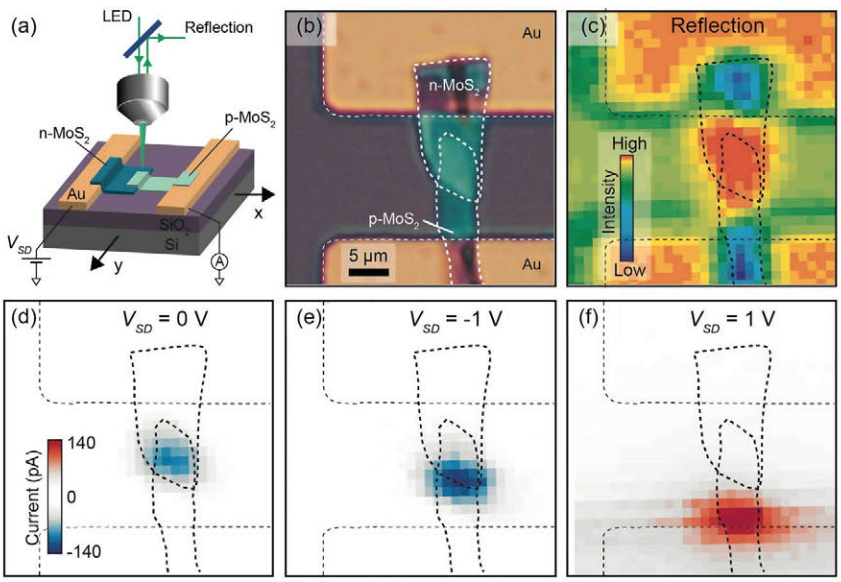

Fig. 6 (a) Sketch of the scanning photocurrent mapping set-up. A fibre-coupled LED (λ = 505 nm, P = 0.6 µW) illuminates the sample which is moved using an xy-micrometer stage. A reflection map allows us to determine the position of the focus. By applying V_{SD} and measuring the photocurrent with respect to the stage position, the spatial origin of the photocurrent can be determined. (b) Optical image of the MoS_2 p–n homojunction. The dashed lines indicate the position of the electrodes and the two flakes. (c) Spatial map of the reflection intensity. (d–f) Photocurrent maps recorded at V_{SD} = 0 V, V_{SD} = −1 V and V_{SD} = 1 V. The photovoltaic response (under short-circuit and reverse bias conditions) originates in the overlap region. Under forward bias (above V_{OC}) conditions, the resistance of the device is determined by the resistance of the leads, which changes due to photoconductivity.

To provide further evidence that the photocurrent is produced only in the junction area, we fabricated another device (Fig. 6b) and recorded scanning photocurrent maps with the set-up sketched in Fig. 6a.[43,44] The device is illuminated with a fiber-coupled LED (λ = 505 nm, the spot diameter is 8 μm) and moved with an *xy*-micrometer stage while simultaneously recording the intensity of the reflected light and the photocurrent. The spatial map of the reflected light intensity allows us to determine the position of the focus.[43] The photocurrent maps in Fig. 6d and e were acquired under short-circuit and reverse bias conditions and reveal that the photovoltaic response exclusively occurs when the overlap region is illuminated. Under forward bias conditions above V_{OC}, the resistance is determined by the resistance of the p-type flake which changes due to photoconductivity (see Fig. 6f).

Summary

In summary, homojunctions based on few-layer MoS_2 have been fabricated and show external quantum efficiencies at 660 nm for different devices between 1.5% and 4.6%. We find that devices in this intermediate thickness regime (15–19 nm) between monolayers and bulk samples behave according to the Shockley-diode model. We have thoroughly analysed the gating effects on the photoresponse and conclude that the thickness of the space charge region decreases with the gate voltage which is correlated with an increase in device performance. We have demonstrated a gate-induced shifting of the maximum power point, J_{SC} and V_{OC}. The device shows fast response times compared with previous studies on MoS_2 layers, which indicates that a vertical design could pave the way to faster MoS_2-based photodetectors. We have shown that devices made from substitutionally doped n-type materials show superior device characteristics than devices made from native MoS_2. The p–n junctions demonstrate the potential of doped MoS_2 for quasi-transparent optical components in light harvesting cells and nanoscale optoelectronics.

Competing financial interest

The authors declare no competing financial interest.

Author contributions

SA Svatek has fabricated the devices and carried out the electrical characterisation. E Antolin generated the software that facilitates the electrical characterisation. DY Lin and TS Ko have fabricated the material. AJ Molina-Mendoz and M Munoz have carried out the AFM characterisation. R Frisenda and C Reuter have carried out the photocurrent mapping. SA Svatek, E Antolin, N Agrait, D Perez de Lara, and AC Castellanos-Gomez have analysed the data. AC Castellanos-Gomez has coordinated the project. All the authors have edited the manuscript and contributed to discussions.

Acknowledgements

S. A. S. and N. A. acknowledge funding from the European Commission through the FP7 ITN MOLESCO (Project Number 606728). E. A. gratefully acknowledges financial support from L'Oréal-UNESCO through the Women in Science program. A. J. M.-M. acknowledges the financial support from MICINN (Spain) through the scholarship BES-2012-057346. D. Y. and T. S. acknowledge the support from the Ministry of Science and Technology of the Republic of China under the MOST 104-2112-M-018-004 and 104-2221-E-018-017. D. P. is thankful for funding from the Spanish Ministry of Economy and Competitiveness through FIS2015-67367-C2-1-P. R. F. thanks the Netherlands Organisation for Scientific Research (NWO) for the financial support through the research programme Rubicon with the project number 680-50-1515. AC-G. acknowledges the support from the BBVA Foundation through the fellowship "I Convocatoria de Ayudas Fundacion BBVA a Investigadores, Innovadores y Creadores Culturales" ("Semiconductores ultradelgados: hacia la optoelectronica flexible"), from the MINECO (Ramón y Cajal 2014 program, RYC-2014-01406), from the MICINN (MAT2014-58399-JIN) and from the Comunidad de Madrid (MAD2D-CM Program (S2013/MIT-3007)), and the European Commission under the Graphene Flagship, contract CNECTICT-604391.

References

1 A. C. Ferrari, F. Bonaccorso, V. Fal'ko, K. S. Novoselov, S. Roche, P. Bøggild, S. Borini, F. H. L. Koppens, V. Palermo, N. Pugno, J. A. Garrido, R. Sordan, A. Bianco, L. Ballerini, M. Prato, E. Lidorikis, J. Kivioja, C. Marinelli, T. Ryhänen, A. Morpurgo, J. N. Coleman, V. Nicolosi, L. Colombo, A. Fert, M. Garcia-Hernandez, A. Bachtold, G. F. Schneider, F. Guinea, C. Dekker, M. Barbone, Z. Sun, C. Galiotis, A. N. Grigorenko, G. Konstantatos, A. Kis, M. Katsnelson, L. Vandersypen, A. Loiseau, V. Morandi, D. Neumaier, E. Treossi, V. Pellegrini, M. Polini, A. Tredicucci, G. M. Williams, B. Hee Hong, J.-H. Ahn, J. Min Kim, H. Zirath, B. J. van Wees, H. van der Zant, L. Occhipinti, A. Di Matteo, I. A. Kinloch, T. Seyller, E. Quesnel, X. Feng, K. Teo, N. Rupesinghe, P. Hakonen, S. R. T. Neil, Q. Tannock, T. Löfwander and J. Kinaret, *Nanoscale*, 2015, **7**, 4598–4810.

2 F. H. L. Koppens, T. Mueller, P. Avouris, A. C. Ferrari, M. S. Vitiello and M. Polini, *Nat. Nanotechnol.*, 2014, **9**, 780–793.

3 L. Britnell, R. V Gorbachev, R. Jalil, B. D. Belle, F. Schedin, A. Mishchenko, T. Georgiou, M. I. Katsnelson, L. Eaves, S. V. Morozov, N. M. R. Peres, J. Leist, A. K. Geim, K. S. Novoselov and L. A. Ponomarenko, *Science*, 2012, **335**, 947–950.

4 E. Fortin and W. M. Sears, *J. Phys. Chem. Solids*, 1982, **43**, 881–884.

5 A. Splendiani, L. Sun, Y. Zhang, T. Li, J. Kim, C.-Y. Chim, G. Galli and F. Wang, *Nano Lett.*, 2010, **10**, 1271–1275.

6 K. F. Mak, C. Lee, J. Hone, J. Shan and T. F. Heinz, *Phys. Rev. Lett.*, 2010, **105**, 136805.

7 P. Tonndorf, R. Schmidt, P. Böttger, X. Zhang, J. Börner, A. Liebig, M. Albrecht, C. Kloc, O. Gordan, D. R. T. Zahn, S. Michaelis de Vasconcellos and R. Bratschitsch, *Opt. Express*, 2013, **21**, 4908.

8 H. J. Conley, B. Wang, J. I. Ziegler, R. F. Haglund, S. T. Pantelides and K. I. Bolotin, *Nano Lett.*, 2013, **13**, 3626–3630.

9 M. M. Furchi, D. K. Polyushkin, A. Pospischil and T. Mueller, *Nano Lett.*, 2014, **14**, 6165–6170.

10 O. V. Yazyev and A. Kis, *Mater. Today*, 2015, **18**, 20–30.

11 X. Cao, Y. Shi, W. Shi, X. Rui, Q. Yan, J. Kong and H. Zhang, *Small*, 2013, **9**, 3433–3438.

12 H. Li, G. Lu, Z. Yin, Q. He, H. Li, Q. Zhang and H. Zhang, *Small*, 2012, **8**, 682–686.

13 C. Zhu, Z. Zeng, H. Li, F. Li, C. Fan and H. Zhang, *J. Am. Chem. Soc.*, 2013, **135**, 5998–6001.

14 H. Heo, J. H. Sung, S. Cha, B.-G. Jang, J.-Y. Kim, G. Jin, D. Lee, J.-H. Ahn, M.-J. Lee, J. H. Shim, H. Choi and M.-H. Jo, *Nat. Commun.*, 2015, **6**, 7372.

15 Y. Gong, J. Lin, X. Wang, G. Shi, S. Lei, Z. Lin, X. Zou, G. Ye, R. Vajtai, B. I. Yakobson, H. Terrones, M. Terrones, B. K. Tay, J. Lou, S. T. Pantelides, Z. Liu, W. Zhou and P. M. Ajayan, *Nat. Mater.*, 2014, **13**, 1135–1142.

16 H. Fang, C. Battaglia, C. Carraro, S. Nemsak, B. Ozdol, J. S. Kang, H. A. Bechtel, S. B. Desai, F. Kronast, A. A. Unal, G. Conti, C. Conlon, G. K. Palsson, M. C. Martin, A. M. Minor, C. S. Fadley, E. Yablonovitch, R. Maboudian and A. Javey, *Proc. Natl. Acad. Sci. U. S. A.*, 2014, **111**, 6198–6202.

17 C. Lee, G. Lee, A. M. van der Zande, W. Chen, Y. Li, M. Han, X. Cui, G. Arefe, C. Nuckolls, T. F. Heinz, J. Guo, J. Hone and P. Kim, *Nat. Nanotechnol.*, 2014, **9**, 676–681.

18 F. Wang, Z. Wang, K. Xu, F. Wang, Q. Wang, Y. Huang, L. Yin and J. He, *Nano Lett.*, 2015, **15**, 7558–7566.

19 Y. Deng, Z. Luo, N. J. Conrad, H. Liu, Y. Gong, S. Najmaei, P. M. Ajayan, J. Lou, X. Xu and P. D. Ye, *ACS Nano*, 2014, **8**, 8292–8299.

20 L. Britnell, R. M. Ribeiro, A. Eckmann, R. Jalil, B. D. Belle, A. Mishchenko, Y.-J. Kim, R. V. Gorbachev, T. Georgiou, S. V. Morozov, A. N. Grigorenko, A. K. Geim, C. Casiraghi, A. H. C. Neto and K. S. Novoselov, *Science*, 2013, **340**, 1311–1314.

21 W. J. Yu, Y. Liu, H. Zhou, A. Yin, Z. Li, Y. Huang and X. Duan, *Nat. Nanotechnol.*, 2013, **8**, 952–958.

22 H.-M. Li, D. Lee, D. Qu, X. Liu, J. Ryu, A. Seabaugh and W. J. Yoo, *Nat. Commun.*, 2015, **6**, 6564.

23 M. S. Choi, D. Qu, D. Lee, X. Liu, K. Watanabe, T. Taniguchi and W. J. Yoo, *ACS Nano*, 2014, **8**, 9332–9340.

24 M. Fontana, T. Deppe, A. K. Boyd, M. Rinzan, A. Y. Liu, M. Paranjape and P. Barbara, *Sci. Rep.*, 2013, 3.

25 J. S. Ross, P. Klement, A. M. Jones, N. J. Ghimire, J. Yan, D. G. Mandrus, T. Taniguchi, K. Watanabe, K. Kitamura, W. Yao, D. H. Cobden and X. Xu, *Nat. Nanotechnol.*, 2014, **9**, 268–272.

26 B. W. H. Baugher, H. O. H. Churchill, Y. Yang and P. Jarillo-Herrero, *Nat. Nanotechnol.*, 2014, **9**, 262–267.

27 A. Pospischil, M. M. Furchi and T. Mueller, *Nat. Nanotechnol.*, 2014, **9**, 257–261.

28 D. J. Groenendijk, M. Buscema, G. A. Steele, S. Michaelis de Vasconcellos, R. Bratschitsch, H. S. J. van der Zant and A. Castellanos-Gomez, *Nano Lett.*, 2014, **14**, 5846–5852.

29 J. Suh, T. Park, D.-Y. Lin, D. Fu, J. Park, H. J. Jung, Y. Chen, C. Ko, C. Jang, Y. Sun, R. Sinclair, J. Chang, S. Tongay and J. Wu, *Nano Lett.*, 2014, **14**, 6976–6982.

30 J. Kang, S. Tongay, J. Zhou, J. Li and J. Wu, *Appl. Phys. Lett.*, 2013, **102**, 12111.

31 M. M. Furchi, A. Pospischil, F. Libisch, J. Burgdörfer and T. Mueller, *Nano Lett.*, 2014, **14**, 4785–4791.

32 S. Y. Wang, T. S. Ko, C. C. Huang, D. Y. Lin and Y. S. Huang, *Jpn. J. Appl. Phys.*, 2014, **53**, 04EH07.

33 A. Castellanos-Gomez, M. Buscema, R. Molenaar, V. Singh, L. Janssen, H. S. J. van der Zant and G. A. Steele, *2D Mater.*, 2014, **1**, 11002.

34 A. Schenk and U. Krumbein, *J. Appl. Phys.*, 1995, **78**, 3185.

35 O. Breitenstein, J. Bauer, A. Lotnyk and J.-M. Wagner, *Superlattices Microstruct.*, 2009, **45**, 182–189.

36 A. Luque and S. Hegedus, *Handbook of Photovoltaic Science and Engineering*, John Wiley & Sons, Ltd, Chichester, UK, 2010.

37 S. Hegedus, D. Desai and C. Thompson, *Prog. Photovoltaics*, 2007, **15**, 587–602.

38 S. Sim, J. Park, J. Song, C. In, Y. Lee, H. Kim and H. Choi, *Phys. Rev. B: Condens. Matter Mater. Phys.*, 2013, **88**, 75434.

39 O. Lopez-Sanchez, D. Lembke, M. Kayci, A. Radenovic and A. Kis, *Nat. Nanotechnol.*, 2013, **8**, 497–501.

40 M. Massicotte, P. Schmidt, F. Vialla, K. G. Schädler, A. Reserbat-Plantey, K. Watanabe, T. Taniguchi, K. J. Tielrooij and F. H. L. Koppens, *Nat. Nanotechnol.*, 2015, **11**, 42–46.

41 D. Kufer and G. Konstantatos, *Nano Lett.*, 2015, **15**, 7307–7313.

42 S. M. Sze, *Physics of Semiconductor Devices*, John Wiley & Sons, 1981.

43 M. Buscema, M. Barkelid, V. Zwiller, H. S. J. van der Zant, G. A. Steele and A. Castellanos-Gomez, *Nano Lett.*, 2013, **13**, 358–363.

44 C.-C. Wu, D. Jariwala, V. K. Sangwan, T. J. Marks, M. C. Hersam and L. J. Lauhon, *J. Phys. Chem. Lett.*, 2013, **4**, 2508–2513.